Hydrodynamics and Mass Transfer around Active and Particles in Dense Gas-Fluidized Beds

Laura Molignano, Maurizio Troiano, Roberto Solimene, Sina Tebianian, Fabrizio Scala, Piero Salatino, Jean-François Joly

Fuel 341 (2023) 127590

Contents lists available at ScienceDirect

Fuel

journal homepage: www.elsevier.com/locate/fuel

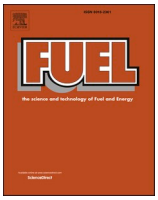

Hydrodynamics and mass transfer around active particles in dense gas-fluidized beds

Laura Molignano [a,b], Maurizio Troiano [a,c], Roberto Solimene [c,*], Sina Tebianian [b], Fabrizio Scala [a,c], Piero Salatino [a,c], Jean-François Joly [b]

[a] Dipartimento di Ingegneria Chimica, dei Materiali e della Produzione Industriale, Università degli Studi di Napoli Federico II, Piazzale Tecchio 80, 80125 Napoli, Italy
[b] Direction Conception Modélisation Procédés, IFP Energies Nouvelles, Rond-point de l'échangeur de Solaize, 69360 Solaize, France
[c] Istituto di Scienze e Tecnologie per l'Energia e la Mobilità Sostenibili, Consiglio Nazionale delle Ricerche, Piazzale Tecchio 80, 80125 Napoli, Italy

ARTICLE INFO

Keywords:
Fluidized bed reactor
Bed expansion
Capacitance probe
Mass transfer
Solid fuel

ABSTRACT

The hydrodynamics of bubbling fluidized beds of Geldart B granular solids operated at ambient temperature and at 500 °C are investigated by uncooled capacitance probes at different gas superficial velocities. Statistical analysis of the time-series of the local bed voidage generates Probability Density Functions (PDF) that display multimodal patterns. A remarkable bimodal character is apparent in the part of the PDF that refers to the emulsion phase when the gas superficial velocity is increased. It is inferred that two phases with different porosity co-exist in the emulsion phase: a lower voidage LV-phase and a higher voidage HV-phase. The link between the LV- and HV-phases as assessed from PDF of capacitance signals and the actual flow patterns induced in the emulsion phase by the bubbles is open to scrutiny.

Along a different path, the influence of the bed hydrodynamics and expansion patterns of the emulsion phase on the gas mass transfer around a freely moving coarse active particle is investigated. To this end, mass transfer-limited reaction experiments are performed, consisting in catalytic oxidation of carbon monoxide at 450 °C over Pt-loaded γ-alumina spheres immersed in the fluidized bed. The mass transfer coefficient around the freely moving active particles is measured and worked out to calculate the particle Sherwood (*Sh*) number. Results obtained from reaction experiments confirm the close relationship between mass transfer and expansion patterns of the emulsion phase, and the need for proper hydrodynamic characterization of the bed. A Frössling-type equation, $Sh = 2{\cdot}\epsilon_e + K{\cdot}(Re_e/\epsilon_e)^{1/2}{\cdot}Sc^{1/3}$, well correlates the results. *Sh* increases with fluidization gas velocity and a best fitting is obtained using the bed voidage of the HV-region of the emulsion phase in the correlation.

1. Introduction

COP27 is calling for an intensification of the nations' commitment and actions toward reduction of carbon emissions as an undelayable path to the established targets of carbon neutrality. The transition toward renewable energy sources and the phase-out of fossil fuels is challenging scientific research to propose novel technologies and optimize existing ones with the aim of making them progressively sustainable and environmentally friendly.

Fluidization technology offers attractive options to the chemical reaction engineer for efficient thermochemical processing of solid fuels via combustion, gasification, and pyrolysis. Fluidized bed combustion of solids is a mature technology, widely practiced worldwide for direct exploitation of biomass, with only moderate effort required to retrofit fossil fuel-based fluidized bed boilers to biomass-fired ones [1]. Gasification is used to convert carbonaceous solids into a high heating value syngas, which can be directly exploited as a fuel or further converted to liquid fuels or chemicals. Although fluidized bed gasification of biomass has been effectively demonstrated [2], there is still room for improvements based on better understanding and control of bed hydrodynamics [3]. Pyrolysis is the thermal decomposition of solids in oxygen-free or oxygen-starving environments. The fast pyrolysis variant, aimed at maximizing yields to bioliquids, is most typically performed in fluidized beds. Fast pyrolysis of biomass represents one of the most promising conversion paths to support the shift from the traditional refinery to the biorefinery-based production of sustainable chemicals and fuels. Selective production of valuable compounds (sugars and oligosaccharides, mono- and oligoaromatics) may only be accomplished by careful control of time–temperature-chemical history to drive conversion along the

* Corresponding author.
E-mail address: roberto.solimene@cnr.it (R. Solimene).

https://doi.org/10.1016/j.fuel.2023.127590
Received 6 December 2022; Received in revised form 20 January 2023; Accepted 22 January 2023
Available online 6 February 2023

Nomenclature

A	surface area [m^2]
C	concentration [kmol/m^3]
Cap	capacitance [F]
D	column diameter [m]
$\widetilde{D}_b$	mean bubble diameter [m]
$\mathscr{D}_{CO}$	diffusion coefficient of carbon monoxide [m^2/s]
d	particle diameter [μm]
$\widetilde{d}$	mean particle diameter [μm]
$Gain$	gain factor of capacitance measuring instrument [F V]
H	height [m]
$\widetilde{H}$	mean height [m]
k	mass transfer coefficient [m/s]
K	fitting parameter in Frössling type correlation [-]
Q	volume flowrate [m^3/s]
r	radius [m]
R	column radius [m]
R_{CO}	reaction rate of carbon monoxide [kmol/s]
S	column cross section [m^2]
t	time [s]
U	gas velocity [m/s]
$\widetilde{U}_{b\infty}$	terminal rise velocity of an isolated bubble [m/s]
V	voltage [V]
x	reaction conversion degree [-]
X	bubble-emulsion phase mass transfer index [-]

Greek Symbols

ϵ	bed voidage [-]
$\widetilde{\epsilon}$	mean bed voidage [-]
$\langle\epsilon\rangle$	spatially averaged bed voidage [-]
ε_0	void dielectric constant [C^2 N^{-1} m^{-2}]
κ	relative dielectric constant [-]
μ	viscosity [N s m^{-2}]
ρ	density [kg/m^3]
$\widetilde{\rho}$	mean density [kg/m^3]
ϕ	sphericity [-]
Σ	capacitance probe geometric characteristic [-]

Dimensionless numbers

Re	Reynolds number [-]
Sc	Schmidt number [-]
Sh	Sherwood number [-]

Subscripts

a	active particle
b	bubble phase
conv	convective diff diffusive
$down$	corresponding to an decreasing trend of voidage
e	emulsion phase
g	gas
HV	high-voidage
LV	low-voidage
$loose$	loose conditions
mf	incipient fluidization
$mode$	mode value
n	column section number
p	bed particle
$pack$	packed conditions
r	radial
s	solid
up	corresponding to an increasing trend of voidage
1	low axial coordinate
2	high axial coordinate

Superscripts

a	active particle
b	bubble phase
e	emulsion phase
in	inlet
$mean$	mean value
$mode$	mode
out	outlet
*	threshold between the LV- and the HV-phases
**	threshold between the HV- and the bubble-phases

prescribed chemical pathway [4]. The rise of a variety of fluidized bed looping processes, headed by the early success of chemical looping combustion (CLC), is opening up novel perspectives for solid fuel conversion, based on the use of solid oxygen carriers to prevent direct contact between fuel and air. CO_2 separation is inherent to CLC processes, so that the energy penalty associated with gas separation is ruled out [5].

Although fluidization technology has been successfully applied to these processes, there are still broad areas of uncertainties regarding bed hydrodynamics, mixing, heat and mass transfer phenomena that are key prerequisites for successful design and operation of fluidized bed converters. Indeed, processes involving fast chemical reactions are more sensitive to bed hydrodynamics, as mixing and mass transfer phenomena become the controlling steps of the conversion [6]. This is the case, for instance, of fluidized bed combustion of biomass [7–9] or fossil solid fuels [10,11], performed at temperatures high enough for intrinsic kinetics not to be the rate-controlling step. For fast heterogeneous chemical reactions, the apparent reaction rate depends on mixing/segregation patterns of the fluidizing gas, determined by the bubbling pattern, and by mass transfer around the active particles.

Mixing/segregation of fluidizing gas in dense gas-fluidized beds of Geldart Group B granular solids is most typically represented according to the simple "two-phase theory" [12]. The bed is composed of two main phases: solids-free bubbles and a dense "emulsion" phase, consisting of a mixture of solid particles and gas. All the gas exceeding the incipient fluidization velocity, U_{mf}, flows across the bed as bubbles, while the emulsion phase is kept at incipient fluidization. Mass transfer between the bubble and the emulsion phases is governed by a gas interchange coefficient, which takes into account gas cross-flow between the phases, as well as diffusional terms. Mass transfer between the bulk of the fluidized bed and an active particle is typically expressed in terms of a Sherwood number according to a Frössling-type correlation [13]:

$$Sh = 2.0 \cdot \epsilon_{mf} + K \cdot \left(\frac{Re_{mf}}{\epsilon_{mf}}\right)^{1/2} \cdot Sc^{1/3} \quad (1)$$

where ϵ_{mf}, is voidage at incipient fluidization conditions, K a fitting parameter, Re_{mf} is the Reynolds number at incipient fluidization referred to the active particle, and Sc is the Schmidt number. In the work of Scala [13], K=0.70. The reference to properties of the bed at incipient fluidization arises from the assumption that active particles mostly reside in the emulsion phase, and by the additional hypothesis that, according to the two-phase theory, the emulsion phase voidage is equal to the bed voidage at incipient fluidization ϵ_{mf}.

There is extensive evidence from the literature that fluidization patterns of dense gas fluidized beds may largely depart from the basic two-phase theory, as regards both the split of fluidizing gas between the bubble and the emulsion phases, and associated bubble flow patterns, and the voidage in the emulsion phase. Key reaction engineering

parameters, like the extent of gas bypass in the emulsion phase, visible bubble flow and bubble rise velocity, mass transfer around fluidized particles, emulsion-bubble interphase mass transfer, are affected accordingly. This has stimulated a continuing effort to diagnose detailed fluidization patterns by application of a broad variety of experimental techniques, aimed at pointwise characterization of bed voidage distribution, particle velocity, particle mass flux and gas velocity.

Visual observation is a straightforward non-intrusive way to obtain information about bed voidage distribution, bubble shape and size, gas velocity. However, its use is limited to transparent-wall units hosting very dilute systems, the outer layer of fluidized beds, and pseudo-2D beds [14]. Visual inspection of the bed may be accomplished at moderate-to-high temperature by infrared [15] or X-ray imaging [16,17]. The latter could be extended to 3D units, although visualization of multiple bubbles and 3D patterns is hampered by the 2D projection of 3D objects. High temporal resolution magnetic resonance imaging (MRI) has been employed to gather 2D images of particle concentration, bubbles and velocity fields in dense fluidized beds [18]. Limitations to the use of this otherwise promising technique are posed by operation at high temperatures, and by the need to develop engineered granular materials that may be considered representative of those fluidized in industrial applications. Tomography can be used as a non-invasive 3D imaging technique. Most electrical capacitance tomography (ECT) systems operate at up to 1000 frames/sec sampling rate. This is an advantage over radioactivity-based tomography, for which sampling frequency is an issue to the benefit of higher spatial resolution. On the other hand, application of ECT in industrial installations is often problematic in high-pressure and/or high-temperature applications in processes carried out in metallic vessels [14]. Radioactive particle tracking (RPT) is an option for investigating particle velocity and bed voidage [19], but an additional technique should be considered to study bubbles phenomenology. Moreover, RPT implementation entails the use of a tailored material resembling real bed properties. Positron emission particle tracking (PEPT) is a non-invasive technique similar to RPT [20].

Among intrusive diagnostics, fast response borescopic probes connected to high speed/resolution cameras can optically access the interior of the dense fluidized bed and provide time-resolved and local information on both bubble and emulsion phases [20]. Post-processing of borescope images may be somehow non-straightforward, entailing the choice of thresholds and imaging parameters that may introduce some bias in the results. Borescopic probes have been used in high temperature dense fluidized beds. However, the technique has not been proved yet in high temperature 3D dense fluidized beds, but only as a non-invasive technique in pseudo-2D units [21]. Instead, optical fiber pyrometry has been successfully used as an intrusive tool in dense fluidized beds operated at 850 °C [22]. Optical probes can be employed for measuring gas distribution, solids velocity and bubble properties, including velocity, in fluidized beds. They have also been used in high temperature units [23]. They provide local measurements; thus, a sufficiently high number of probes must be adopted to gather a 3D description of the dense fluidized bed.

Capacitance probes are similar to optical probes as they allow the investigation of several aspects of the dense fluidized bed, they can be easily implemented and signals are not difficult to interpret. Small measuring volumes [24], fine temporal resolution, relatively low costs and possible applicability in industrial units represent other positive features of this technique [14]. Needle capacitance probes [24] are usually utilized in fluidized beds since the miniaturized design causes very little disturbances of the flow. This aspect has been proved in the study of Tebianian *et al.* [25]: the use of a 4 mm OD probe produced slight qualitative variations on voidage distribution, and, quantitatively, the average voidage only changed within 2 % with reference to the condition where the probe was absent. A customized uncooled capacitance probe has been designed and manufactured for application to fluidized beds operated at high temperature [26]. The response of the probe can be fast enough to follow voidage fluctuations up to 2 kHz [14].

Diagnosis based on gas pressure measurements can be either intrusive or not. Pressure probes are cheap and relatively easy to manufacture, and therefore widely applied in fluidized beds. They can give an estimate of bed bulk density or average bed height. When pressure is sampled at sufficiently high frequency, the pressure fluctuation signal can yield much more information about bed hydrodynamics. In fact, from pressure signals it is possible to obtain details about local bubble passage and non-local compression waves, which originate from bubble generation, bubble coalescence, bubble eruption, and gas flow fluctuations [14]. Time-resolved measurements concern single-point absolute pressures or pressure differences between two points. Even when suitable sensors are used, measurements can easily be distorted due to resonance effects from the connection tubes, signal dampening caused by connection tubes small diameters, disturbances from purge flows, particles entering the probe, probe positioning relative to the bed. Moreover, interpretation of pressure signals is not straightforward [14]. Particle pressure can be measured separately from gas pressure by adding some bypass tubing to the chamber of the sensor covered by the diaphragm [27]. Acoustic measurements can be an alternative to pressure taps, especially in industrial units operated at high pressure. However, they are only used to obtain qualitative information about the state of fluidization [14].

The combined use of the above-mentioned techniques has greatly contributed to advance towards a more realistic description of the fluidized beds, shedding light, among the others, on bubbling patterns: shape and size of bubbles, wake extension and associated flow [19], particle fingering and raining from the roof of the bubble, and associated bubbles splitting [28], formation of clouds, coalescence, bubble-induced large scale motion and solids mixing [29].

Departures of the voidage in the emulsion phase with respect to that at incipient fluidization conditions have been observed for Geldart A, AB [30], B [31] and D [32] groups solids. Cui *et al.* [33] underlined that both Geldart A and B solids exhibit a distribution of emulsion phase voidages, the mean void fraction of the emulsion-phase in a freely bubbling bed being remarkably different from that at incipient fluidization. Yates *et al.* [16] demonstrated, for groups A and B of Geldart classification, that voidage around gas bubbles decreases exponentially to that of the emulsion phase far from the bubble, and that there is no sharply defined boundary between bubble, cloud, and emulsion. Andreux and Chaouki [34] identified thresholds to separate the dense phase, the cloud and bubbles by adopting a statistically-based approach.

Increasing the temperature affects the gas–solid distribution in a way that cannot be simply predicted by accounting for gas properties variation (i.e., density and viscosity) [35,36]. Interparticle forces may play an important role under certain conditions, providing one key for the effect of temperature. Shabanian and Chaouki [37] extensively surveyed the literature regarding the effects of temperature, pressure and interparticle forces on the hydrodynamic behavior of Geldart A, B and D solids. Altogether, it is concluded that the effect of temperature on bed hydrodynamics is still poorly characterized and understood, and this may jeopardize design and operation of industrial-scale fluidized bed converters operated at moderate-to-high temperature.

In the present study, the voidage distribution in a dense bubbling fluidized bed of particles of a solid material belonging to group B of Geldart classification is investigated. Capacitance probes have been chosen due to their favourable features as compared with alternative diagnostics in terms of ease of operation and signal interpretation, temporal resolution, cost, applicability in severe high temperature environments, and applicability in industrial units. Custom-made capacitance probes have been manufactured and fitted to a fluidized bed unit, with the measuring volume placed at different radial/axial positions in the column. The signals have been elaborated using a statistical approach and a detailed time-resolved analysis. Experiments have been performed both at room temperature and high temperature conditions. The measurements were also compared with mean bed voidage values calculated with equations from the two-phase theory model. A dedicated

experimental campaign has been directed to characterize the influence of gas flow distribution on the mass transfer around active particles when a fast chemical reaction, namely the catalytic oxidation of carbon monoxide at 450 °C over Pt-loaded alumina spheres, takes place.

2. Experimental

2.1. Apparatus

Two types of experiments have been carried out: a) hydrodynamic characterization of the dense fluidized bed; b) measurement of the mass transfer coefficient between the bed and active catalyst particles during fast catalytic oxidation of CO.

A stainless steel 3" diameter (schedule 40: ID 77.92 mm) and 1300 mm high column, operated as atmospheric bubbling fluidized bed (Fig. 1), has been used for both the experiments. The fluidization gas distributor belongs to the low pressure drop type. It is a 2 mm triangular pitch perforated plate placed under two steel 40 μm passing light meshes, providing the major contribution to the distributor pressure drop. The average pressure drop across the gas distributor is 173 Pa, and its ratio to the pressure drop across bed solids ranges between 8 and 11 %, depending on gas superficial velocity. The windbox is a 225 mm high stainless steel column filled with ceramic rings to equalize the gas flow. The fluidization column and bed material are heated by two semi-cylindrical 2.4 kW ceramic ovens, and the reactor is thermally insulated. Bed temperature is kept at the set point by a PID control unit regulating the ovens. Gases are fed to the column via high-precision digital mass flowmeters/controllers. The exhaust from the reactor is vented. The column presents 8 different 3/8" diameter (schedule 40: ID 12.4 mm) ports that provide access to pressure/temperature and capacitance probes. In Fig. 1 only the ports which have been used for the experiments are represented. One port is located under the gas distributor. The others consist in lateral accesses placed at different vertical positions along the column, at distances above the distributor plate of 0.01, 0.06, 0.1, 0.14, 0.18, 0.34 and 0.95 m. Each measurement probe is connected to its data acquisition module and signals are acquired simultaneously on LabVIEW through a laboratory computer.

2.2. Materials

Grey quartz sand has been used as bed material in the hydrodynamic characterization experiments, whose properties are reported in Table 1. The material is conditioned and double sieved in a relatively narrow particle size range of 420–590 μm. The arithmetic mean diameter, $\widetilde{d}_p$, is computed from the 420–590 μm sieve range, whereas the representative diameter is back calculated from the empirical equation of Wen and Yu (1966), starting from the value of the incipient fluidization velocity, U_{mf}, measured at ambient temperature [38]. The sphericity of grey quartz, ϕ, is obtained as an adjustable parameter from Ergun equation [38], starting from values of U_{mf} and voidage at incipient fluidization, ϵ_{mf}, measured at ambient temperature. This procedure, suggested by Knowlton [39], has been adopted by Formisani *et al.* [40]. ϵ_{mf} of quartz at ambient temperature is considered equal to the loose bed voidage, according to Grace *et al.* [41]. The loose bed voidage, as well as the packed bed voidage, ϵ_{pack}, is measured in a graduated cylinder of 500 ml so that wall effects could be minimized [42]. ϵ_{mf} at 500 °C is calculated from Ergun equation, where all the variables are measured or calculated at the temperature of interest and ϕ is the one back calculated at ambient conditions.

Experiments aimed at measurement of mass transfer under reactive conditions have been performed using a batch of 2 $\%_{w/w}$ Pt catalyst supported on γ-alumina dispersed in the inert bed material, whose properties are described in Table 1. The catalyst is selected among those tested by Scala [13]. Catalyst size is obtained by measuring each particle diameter with a caliper and, then, computing the arithmetic mean over all the measurements. Arithmetic mean density and diameter of particles are, thus, reported in Table 2.

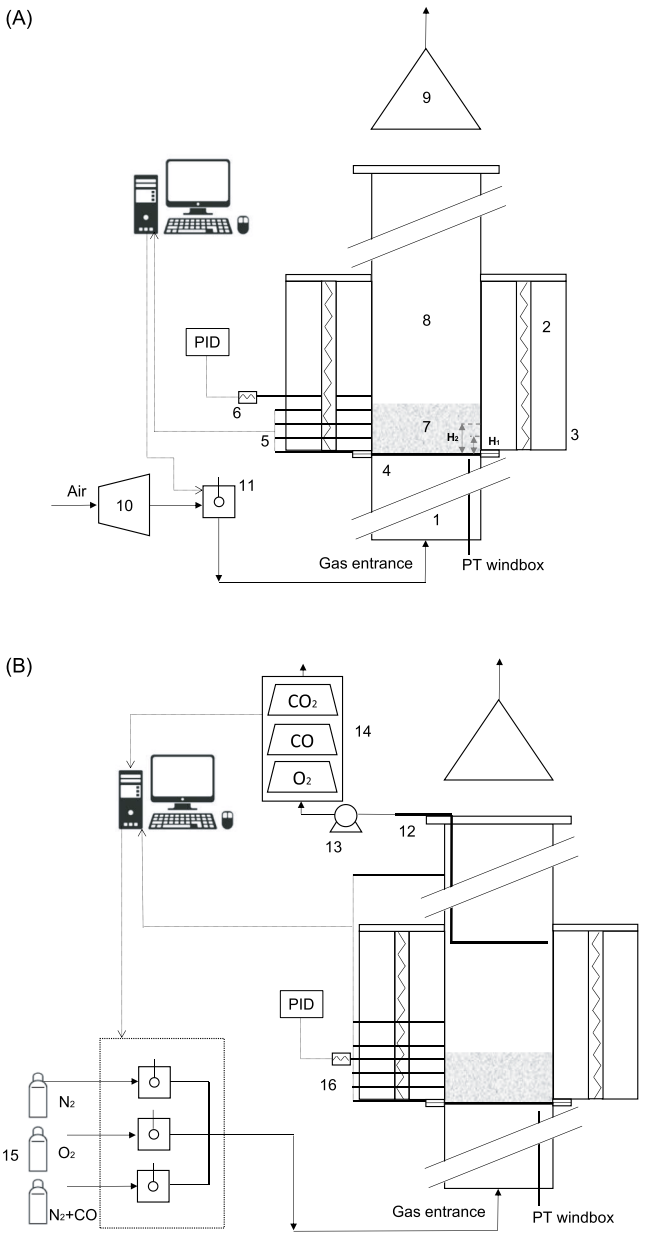

Fig. 1. (A) Experimental apparatus for bed voidage measurement experiments; (B) Experimental apparatus for reactive experiments. 1) Windbox; 2) electrical furnaces; 3) ceramic insulation; 4) gas distributor; 5) column ports for pressure transducers, thermocouples and capacitance probes; 6) thermocouple for oven PID controller; 7) bed solids; 8) fluidization column; 9) hood; 10) compressor; 11) air flowmeter; 12) gas suction probe; 13) membrane pump; 14) gas analyzers; 15) gas cylinders; 16) column ports for pressure transducers and thermocouples. H_1 = 0.06 m and H_2 = 0.1 m represent the axial location of the probes in terms of distance from the distributor. PT windbox: pressure transducer placed under the gas distributor.

2.3. Hydrodynamic characterization of the dense fluidized bed

2.3.1. Experimental procedure

Fig. 1A reports an outline of the experimental test rig used for bed voidage measurements with capacitance probes. Grey quartz sand is fluidized in bubbling regime with air at ambient temperature and at 500 °C. The same excess gas superficial velocities with respect to

Table 1
Properties of the inert bed material.

Material	Grey quartz sand
Sieve range, $d_p[\mu m]$	420–590
$\widetilde{d}_p[\mu m]$	505
Representative $d_p[\mu m]$	517
$\phi[-]$	0.64
$\rho_p[\frac{kg}{m^3}]$	2650
$\rho_{loose}(20^\circ C)[\frac{kg}{m^3}]$	1389
Geldart group	B
$U_{mf}(20^\circ C)[\frac{m}{s}]$	0.207
$U_{mf}(450^\circ C)[\frac{m}{s}]$	0.115
$U_{mf}(500^\circ C)[\frac{m}{s}]$	0.119
$\epsilon_{pack}(20^\circ C)[-]$	0.44
$\epsilon_{mf}(20^\circ C)[-]$	0.48
$\epsilon_{mf}(500^\circ C)[-]$	0.49
$\kappa_s(20^\circ C)[-]$	3.5
$\kappa_s(500^\circ C)[-]$	6.2

Table 2
Properties of catalyst particles used in reaction experiments.

Mean size, $\widetilde{d}_a[mm]$	Particle density, $\widetilde{\rho}_a[\frac{kg}{m^3}]$	Type
3.9 ± 0.11	1128 ± 109.4	2 % w/w Pt on γ-alumina spheres provided by Süd-Chemie

incipient fluidization, in the range of 0.01–0.35 m/s, are applied for the two temperatures. Additional excess gas velocities are tested at 500 °C, up to $U-U_{mf} = 0.68$ m/s. The amount of bed material loaded in the column is such that the packed bed aspect ratio, H/D, is 1.6.

The capacitance signal is recorded at two different axial positions inside the bed (H_1 and H_2), which are sufficiently far from both the distributor and the splash zone (distance from the distributor plate of 0.06 and 0.1 m, respectively) to avoid end-effects. At each bed height, the capacitance probe is placed at three radial positions, namely bed center, mid-radius and wall, corresponding to r/R ratios of 0, 1/2 and 7/9, respectively. For each run, capacitance signals are acquired and postprocessed using LabVIEW software for 180 s with a sampling frequency of 1 kHz. At low velocity, the acquisition time is shortened to 120 s to avoid the establishment of temperature gradients inside the bed.

2.3.2. Capacitance probes and signal processing

The capacitance probe is a capacitor based on the typical needle-type cylindric design [24]. The measuring volume of the probe is defined by the electric field, which establishes between the protruding sensor needle and the outer diameter of the ground electrode. The capacitance of the medium that passes through the pseudo conical-shaped electric field is measured based on the sensing volume geometry, Σ, and on the relative dielectric constant of the medium, κ. The sensor is connected via a triaxial line consisting of central, guard [26,43], and ground electrodes to a customized amplifier. The amplification and rectification of the sensor AC voltage yields to a DC signal voltage, V, that corresponds to the output of the instrument. The signal shows inverse proportionality with the capacitance, Cap, through the gain factor of the amplifier:

$$V = Gain/_{Cap} = Gain \Big/ (\kappa\varepsilon_0\Sigma) \tag{2}$$

where ε_0 is the void dielectric constant. The present study is performed with a custom-made uncooled capacitance probe resistant to high temperatures. Central sensor, guard and ground cylinders are made of stainless steel, while the electric insulation is obtained by using ceramic tubes in the probe section immersed in the hot bed [26], and plastic tubes in the cold end of the probe. The ground tube outer diameter is 6.75 mm, the needle length and diameter are 5.7 mm and 1.6 mm, respectively. The volume of the measured domain can be estimated around 130 mm^3, calculated as mean value of the volume associated to a cylinder and to a cone. The connection of the central and guard electrodes to the customized amplifier through a low noise coaxial cable limits any disturbances on the measured signal.

The greatest difficulty in designing the probe is to deal with different thermal expansions of steel and ceramic tubes. Therefore, the tubes are connected with refractory glue close to the sensing volume so that they can freely expand to the side opposite to the probe tip without altering the sensing volume geometry at high temperature. The refractory glue also prevents particles from entering between the cylinders. Fig. 2 resumes the stages of cylinders assembling. When the probe is inserted in the empty fluidization column, air signal is slightly lowered due to the column walls, but its average value never goes under 96 % of the signal recorded in free air outside the column. The value in air at 500 °C is recorded after heating the probe with fluidized quartz sand and draining the bed. The small variation of the signal from ambient temperature to 500 °C can be due to a small radial expansion of the ground tube, thus capacitance increase and voltage decrease. The impact of this variation on actual measurements is negligible.

Accuracy of bed voidage measurement by capacitance probes is critically dependent on the knowledge of the correct material relative permittivity. Relative dielectric constants, κ_s, reported in literature for grey quartz sand could be different from that of the sample adopted in the present study due to sensitivity to several parameters [24]. Therefore, κ_s for grey quartz sand was measured *in situ*, in dedicated tests performed keeping the bed at incipient fluidization. The general relationship between κ_s and the emulsion phase voidage ϵ is given by:

$$\kappa = \kappa_s \cdot (1-\epsilon) + \epsilon \tag{3}$$

In the present case κ was measured under incipient fluidization conditions, κ_{mf}, and averaged over multiple measurements. The resulting κ_s value at room temperature and at 500 °C is reported in Table 1. The relative dielectric constant of grey quartz sand increases with temperature.

The time-resolved local relative permittivity of the fluidized bed obtained from Eq. (2) is further worked out, through Eq. (3), to obtain

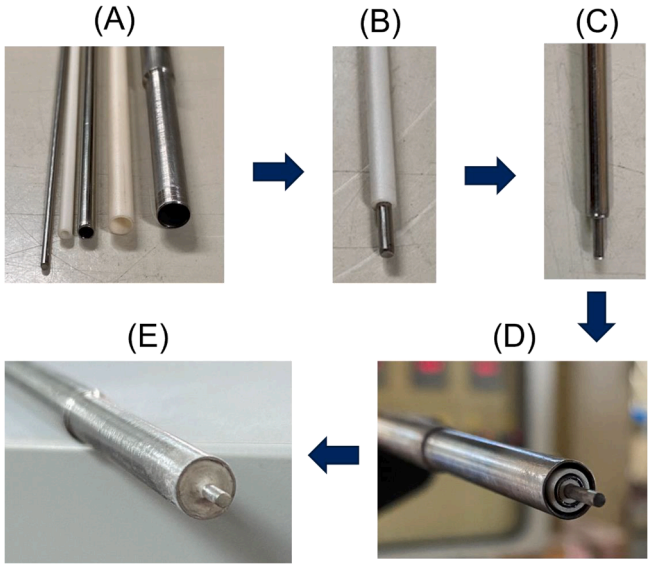

Fig. 2. The capacitance probe. (A) From left to right: needle-type central sensor, inner ceramic tube, guard tube, outer ceramic tube, ground tube; (B) needle-type central sensor and ceramic tube assembly; (C) guard tube addition; (D) complete assembly; (E) refractory glue addition.

the time-series of local bed voidage. These time series have been further analyzed by a statistical method to generate Probability Density Functions (PDF) of the local voidage, using the Matlab software. The Freedman-Diaconis rule [44] has been used to select the optimal bin width, so that the resulting PDF is not affected by bed voidage values and acquisition time. The main features of the PDFs have been compared at different superficial gas velocities, axial/radial coordinate of capacitance probe sensing volume and temperatures.

Pointwise voidage measurements are compared with the fluidized bed mean voidage, $\widetilde{\epsilon}$, calculated as:

$$\widetilde{\epsilon} = 1 - \frac{H_{mf}(1-\epsilon_{mf})}{\widetilde{H}} \tag{4}$$

where $\widetilde{H}$ is the mean bed height. Direct measurement of $\widetilde{H}$ is problematic under the operating conditions of the test due to the rapidly fluctuating level of the bed surface. An estimate of $\widetilde{H}$ can be obtained based on the two-phase theory from the volume fraction of the bed occupied by bubbles $\widetilde{\epsilon}_b$ as:

$$\left(\widetilde{H} - H_{mf}\right)\Big/ H_{mf} = \widetilde{\epsilon}_b/(1-\widetilde{\epsilon}_b) \tag{5}$$

valid for group B and D powders, under the assumption that the dense phase voidage does not depart much from ϵ_{mf} and bed expansion is dominated by the hold-up of bubbles [45]. When the visible bubble flow and the mean bubble velocity are considered, Eq. (5) becomes

$$\left(\widetilde{H} - H_{mf}\right)\Big/ H_{mf} = \left(U - U_{mf}\right)\Big/ \widetilde{U}_{b\infty} \tag{6}$$

where $\widetilde{U}_{b\infty}$, the mean bubble rise velocity with respect to the emulsion phase, is estimated for a characteristic bubble diameter, $\widetilde{D}_b$, which, in the present case, is the bubble diameter at mid-height of the fluidized bed, estimated according to Darton *et al.* [46].

The local capacitance probe measurements are integrated first over the whole cross section under axisymmetric assumption and then over the bed height. The integration is performed by dividing the column section into three concentric subsections, S_n:

$$\langle\epsilon\rangle_r = \frac{\sum_{n=1}^{3}\epsilon_n^{mean}S_n}{S} \tag{7}$$

with n representing the subsection number. The averaging over the height is performed computing the arithmetical mean of $\langle\epsilon\rangle_{r,1}$ and $\langle\epsilon\rangle_{r,2}$, which refer to H_1 and H_2 coordinates.

2.4. Measurement of the mass transfer coefficient under reactive conditions

2.4.1. Experimental procedure

Fig. 1B shows the experimental apparatus equipped for the reaction experiments. The amount of bed material loaded in the column is the same as in the experiments described in paragraph *2.3*. The first three measurement ports, starting from the distributor, are equipped with gas pressure transducers to check the fluidization quality, and with K-type thermocouples to verify bed temperature uniformity. The fourth port is employed for the PID thermocouple. Ports from the fifth to the seventh host K-type thermocouples to measure the temperature in the splash zone and in the freeboard of the reactor. The gas feeding at the desired composition (CO 830 ppm_v, O_2 5 $\%_{v/v}$, N_2) is obtained by mixing three streams of gas supplied from cylinders containing high purity N_2, O_2, and a N_2-CO mixture (30 $\%_{v/v}$ CO), respectively, metered by three gas flowmeters calibrated with a bubble flowmeter. A stainless-steel L-shape probe is inserted from the top of the column in order to convey a known fraction (60 l/h) of the exit gas directly to the gas analyzers. Gas sampling is performed at a distance from the top section of the bed of about 450 mm. The probe is a 4 mm ID tube, plugged at the end of the horizontal section inserted in the column. Gas is sampled through five 1 mm diameter holes, uniformly distributed along the horizontal section of the tube so as to measure the mean gas composition over the column cross-section. The analyzers measure on-line O_2, CO and CO_2 concentrations in the exhaust gases. The measuring ranges of the CO and CO_2 analyzers used in the experiments are 10,000 and 2000 ppm_v, respectively. They are calibrated at the beginning of each lab-work day with specific calibration cylinders for CO (1000 ppm_v CO) and CO_2 (200.2 ppm_v CO_2). The analyzers are also employed to verify the composition of the gas mixture at the column feeding port, via a valve that deviates a small gas flowrate to the analyzers.

Experiments are carried out at a bed temperature of 450 °C. A preliminary check was directed to verify that contributions to CO oxidation arising from homogeneous gas phase reactions and from sand or wall catalyzed reactions could be neglected at the selected temperature. Possible segregation of catalyst particles was ruled out after dedicated cold tests, at scaled operating conditions, in which the bed solids and the catalyst particles were fluidized in a Plexiglas column to allow visual inspection. External diffusion around the catalyst particle was considered as the only controlling resistance for CO oxidation at 450 °C, as widely verified by Venderbosch *et al.* [47] and by Scala [13].

The gas superficial velocity was varied in the range 0.215 m/s $< U <$ 0.815 m/s, corresponding to fully established freely bubbling fluidization regime. A preliminary analysis of the pressure time series in the frequency domain highlights a dominant characteristic frequency in the range 2–3 Hz, typical of bubbling conditions and far from slugging [48].

The tests were performed by injecting a batch of catalyst particles in the fluidized bed from the top of the column. The mass of the catalyst was selected so as to establish a conversion degree of carbon monoxide, x_{CO}, of about 5 %, corresponding to nearly differential operation. Accordingly, uncertainties associated with detailed fluid-dynamics of the bed are minimized. The mass of catalyst particles increases with increasing flowrate due to the decrease of the gas residence time. After catalyst feeding, concentrations of CO, CO_2 and O_2 in the exhaust gases are measured by the analyzers and signals acquired using the LabVIEW software at a sampling rate of 1 Hz during the transient and the steady-state condition.

2.4.2. Analysis of data

Analysis of the experimental data assumes that the catalyst particles only reside in the dense phase of the fluidized bed. This assumption is based on the experimental evidence reported in the literature, considering that catalyst particles are coarser than the inert bed solids. Bed fluid dynamics is modelled according to the two-phase fluidization theory: gas in the bubble phase is in plug flow; gas and solids in the emulsion phase are well stirred. Gas perfect mixing in the emulsion phase is a direct consequence of the small conversion degree. The bubble–emulsion phase mass transfer coefficient is calculated according to Sit and Grace [49] and, consequently, the bubble–emulsion phase mass transfer index, X, is derived. Under external diffusion control (assuming a vanishing CO concentration at the surface of the active particle) the total reaction rate in the dense phase of the fluidized bed, R_{CO}, can be expressed as

$$R_{CO} = A_a \cdot k_g \cdot C_{CO}^e \tag{8}$$

A_a being the total external surface of the spherical catalyst particles and k_g the emulsion gas-to-active particle mass transfer coefficient. Below, the material balances on CO in the bubble (Eq. (9)) and dense phase (Eq. (10)), and at the reactor outlet (Eq. (11)) are reported under the above assumptions:

$$C_{CO}^b = C_{CO}^e + \left(C_{CO}^{in} - C_{CO}^e\right)\cdot e^{-X} \tag{9}$$

$$A_a \cdot k_g \cdot C_{CO}^e = Q\left(C_{CO}^{in} - C_{CO}^{out}\right) \tag{10}$$

$$Q \cdot C_{CO}^{out} = Q_{mf} \cdot C_{CO}^e + \left(Q - Q_{mf}\right)\cdot C_{CO}^b \tag{11}$$

where the unknowns are represented by k_g, CO concentration in the bubble phase, C^b_{CO}, and in the emulsion phase, C^e_{CO}. Q represents the volumetric flowrate. By substituting Eq. (9) in Eq. (11), C^e_{CO} can be expressed as a function of CO concentration at the inlet, C^{in}_{CO}, and outlet, C^{out}_{CO}. $x_{CO} = \frac{C^{in}_{CO} - C^{out}_{CO}}{C^{in}_{CO}}$ is the overall CO conversion degree in the reactor, as measured in the experiments, and the Sherwood number is defined as $Sh = \frac{k_g d_a}{\mathscr{D}_{CO}}$, where d_a is the diameter of the active particle and $\mathscr{D}_{CO}$ is the diffusion coefficient of CO. By introducing these two terms in Eq. (10) and substituting the expression for C^e_{CO} previously derived, the equation for the calculation of Sh number can be finally written:

$$Sh = \frac{d_a A_r}{\mathscr{D}_{CO} A_a} \cdot \frac{U_{mf} + (U - U_{mf}) \cdot (1 - e^{-X})}{(1 - x_{CO}) - \frac{U - U_{mf}}{U} \cdot e^{-X}} \cdot x_{CO} \tag{12}$$

where A_r is the reactor cross section.

3. Results and discussion

3.1. Bed voidage measurements by capacitance probes

Fig. 3 represents selected time-series of local bed voidage recorded at ambient temperature at different excess gas superficial velocities, with the capacitance probe inserted at the column center at H_1. At the smaller gas superficial velocity (Fig. 3A), the bed voidage oscillates around a dominant value corresponding to incipient fluidization. The minimum voidage is close to packed conditions, whereas upward spikes mark the passage of bubbles. As gas superficial velocity is increased (Fig. 3B) the passage of bubbles becomes more frequent, though a "baseline" representative of the emulsion phase may still be recognized, around a voidage slightly higher than ϵ_{mf}. Further increase of the superficial gas velocity (Fig. 3C) makes the signal more chaotic. Time-resolved voidage signals obtained at 500 °C and at different excess superficial gas velocities are reported in Fig. 4. The general qualitative features of the voidage time-series at high temperature resemble those observed at room temperature.

Time-resolved bed voidages corresponding to the gas velocities, temperatures, and radial/axial locations of the capacitance probe tested indicate that:

- local bed voidages at 500 °C, averaged over the entire acquisition time, are larger than those measured at ambient temperature for any given excess gas superficial velocity $U - U_{mf}$ when the sensing volume of the probe is placed at the column center and mid-radius, whereas they are similar when the probe is located close to the wall.
- Maxima in the voidage signals slightly decrease as temperature is increased, a feature that could be due to smaller bubbles or more solids occupying the bubble volume at 500 °C. Hilligardt and Werther [31] reported that an increase in bed temperature results in a decrease of bubble size. Shabanian and Chaouki [37] concluded that,

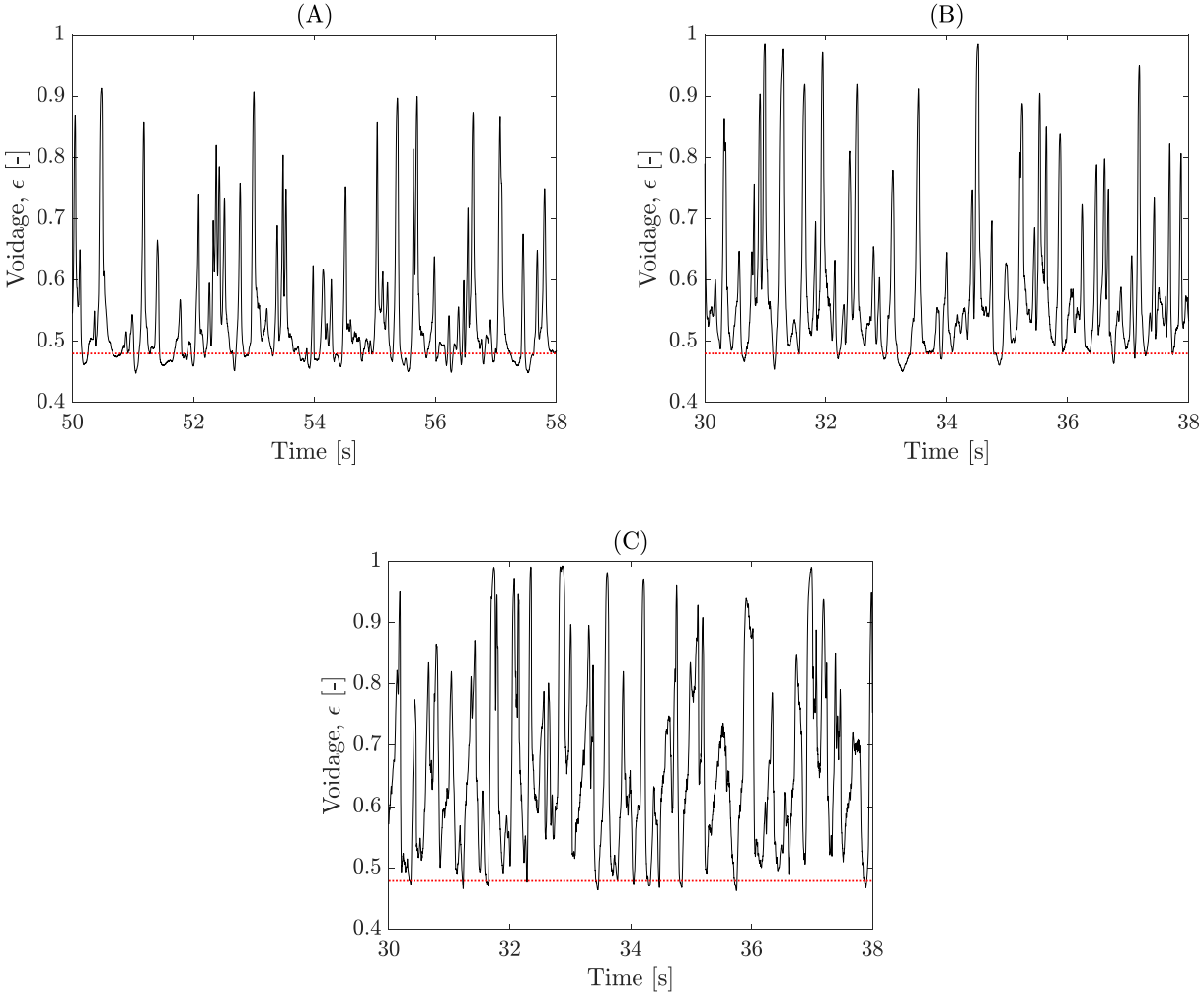

Fig. 3. Time-resolved voidage signals. Probe radial location:r/R = 0; probe level: H_1, T: ambient. (A) $U - U_{mf} = 0.01 m/s$; (B) $U - U_{mf} = 0.05 m/s$; (C) $U - U_{mf} = 0.25 m/s$. The dotted horizontal line in red represents ϵ_{mf} value. (For interpretation of the references to colour in this figure legend, the reader is referred to the web version of this article.)

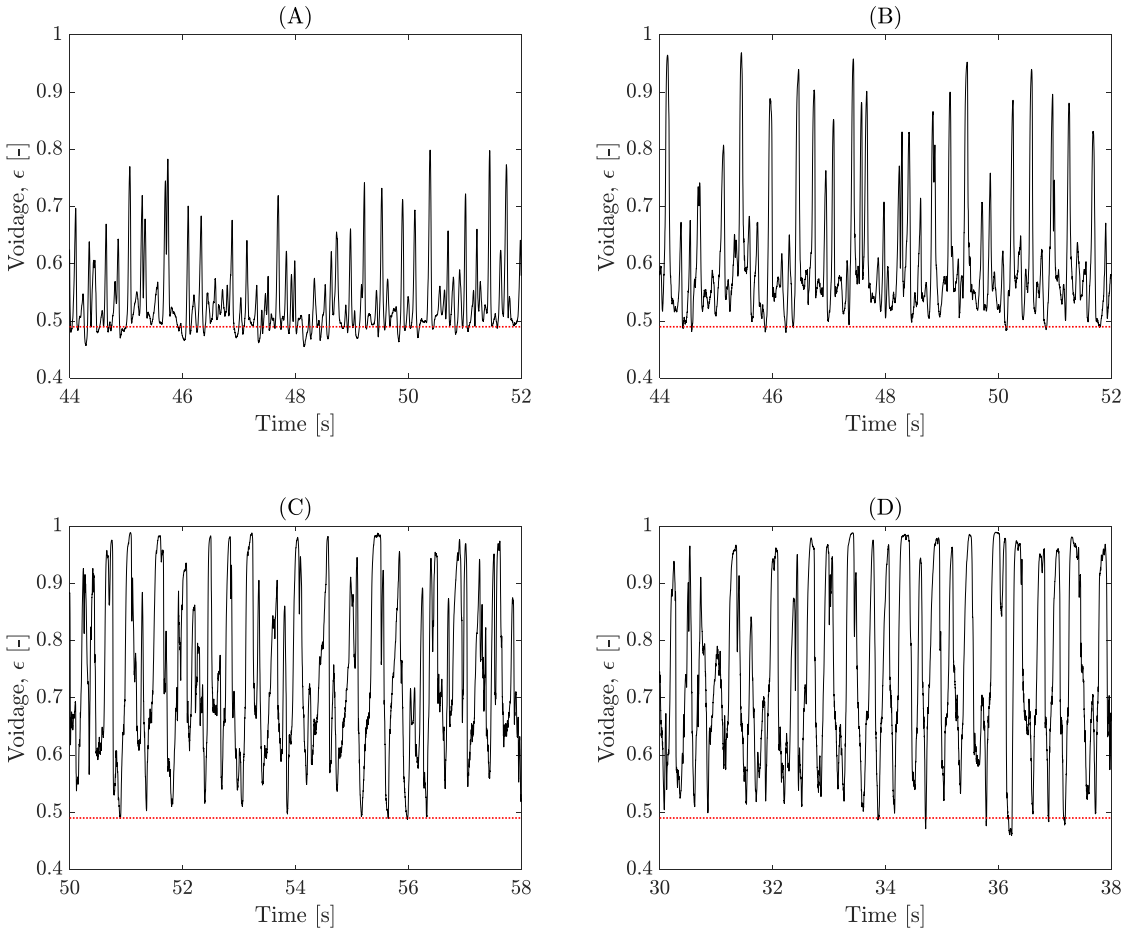

Fig. 4. Time-resolved voidage signals. Probe radial location: r/R = 0; probe level: H_1, T: 500 °C. (A) $U-U_{mf} = 0.01m/s$; (B) $U-U_{mf} = 0.05m/s$; (C) $U-U_{mf} = 0.25m/s$; (D) $U-U_{mf} = 0.5m/s$. The dotted horizontal line in red represents ϵ_{mf} value. (For interpretation of the references to colour in this figure legend, the reader is referred to the web version of this article.)

for Geldart B solids, there is a tendency of gas to interstitially pass through the particles at high temperature.

- Minima in the voidage signals show the opposite behavior, increasing as temperature increases. It is plausible that values at ambient temperature fall around the packed bed voidage, as measured in the graduated cylinder, and reported in Table 1. As temperature is increased, even the packed bed voidage could increase with respect to ambient conditions [40].
- The mean local bed voidage is greater at the top level H_2 both at room and at high temperature. The same trend is observed for the maximum voidage. Instead, the baseline voidage levels are nearly the same at the two axial coordinates for both temperatures.
- No noticeable differences arise for minimum and maximum values of local bed voidage measured along the radial coordinate, for the tested material. Minima are nearly constant with gas velocity; in agreement with Cui *et al.* [33], the growth of maximum value is exponential for low values of $U-U_{mf}$ and the voidage remains nearly constant at higher gas velocities.

Fig. 5 reports the time and spatially-averaged values of bed voidage as a function of the excess gas superficial velocity. Averaging of local experimental data according to Eq. (7), followed by the arithmetic mean between values at H_1 and H_2, shows departures from the mean bed voidage, expressed by Eq. (6), that never exceed 10 %.

Interpretation of the voidage time series is better accomplished by means of the statistical approach presented hereinafter. To this end, the time series of the local voidage have been worked out to yield the PDF

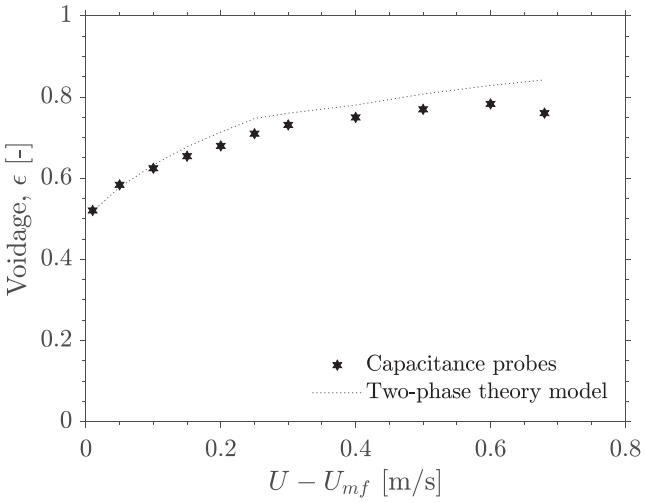

Fig. 5. Time- and space-averaged bed voidage as a function of excess gas superficial velocity. T: 500 °C. Data points: measurements by capacitance probes; line: Eq. 4.

reported in Fig. 6, for ambient temperature, and in Fig. 7, for the data set at 500 °C, at different locations in the bed.

Analysis of the PDF turns out to be helpful to infer key features of bed hydrodynamics [50]. As the bed is operated under nearly incipient

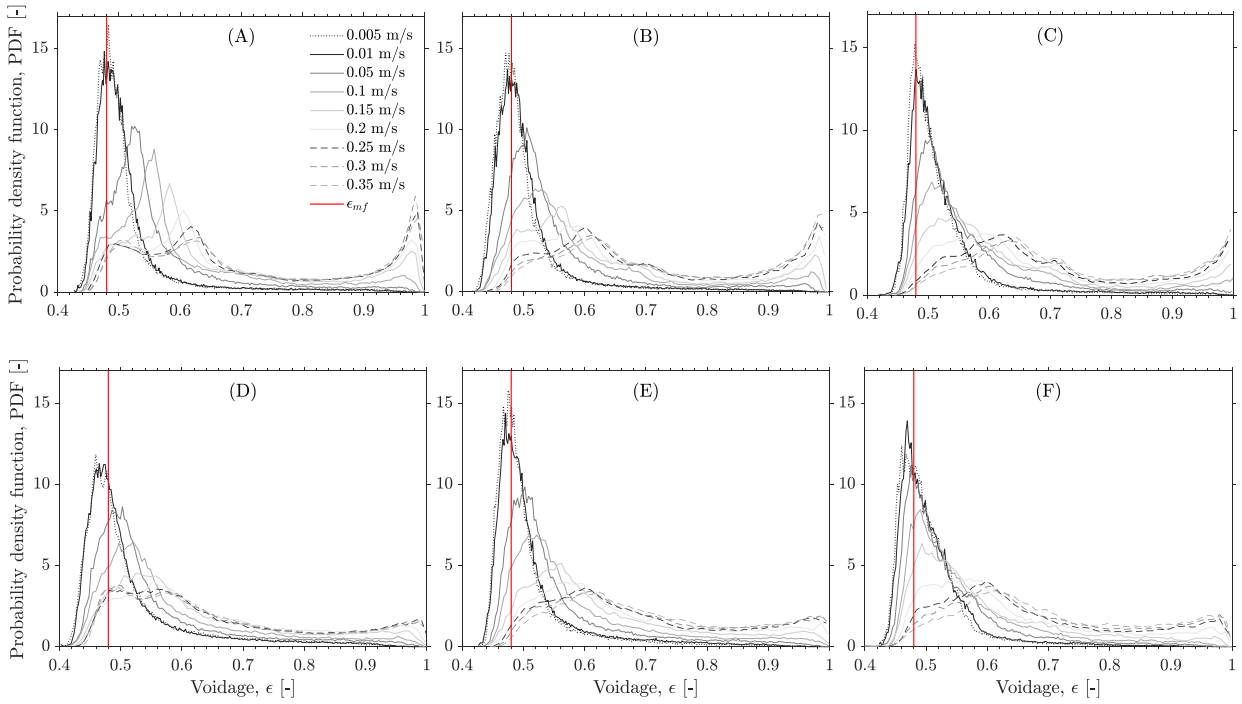

Fig. 6. Probability density functions of the local voidage at ambient temperature for different $U - U_{mf}$ and probe locations. Probe level $H_2 = 0.1$ m from distributor: (A) Center; (B) Mid-radius; (C) Wall. Probe level $H_1 = 0.06$ m from distributor: (D) Center; (E) Mid-radius; (F) Wall.

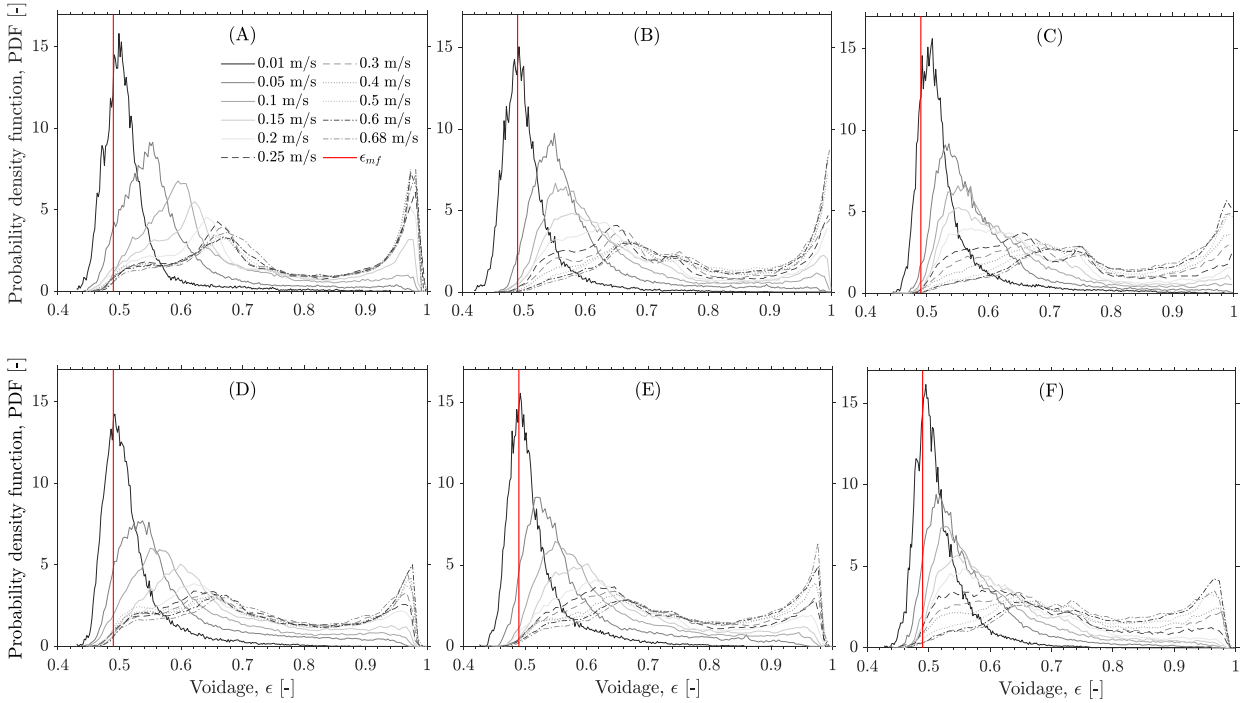

Fig. 7. Probability density functions of the local voidage at 500 °C for different $U - U_{mf}$ and probe locations. Probe level $H_2 = 0.1$ m from distributor: (A) Center; (B) Mid-radius; (C) Wall. Probe level $H_1 = 0.06$ m from distributor: (D) Center; (E) Mid-radius; (F) Wall.

fluidization conditions ($U \cong U_{mf}$), the PDF displays a slightly skewed unimodal trend, with a voidage modal value $\epsilon_{mode} \cong \epsilon_{mf}$. Indeed, the bed is mainly constituted by the emulsion phase, characterized by a fairly narrow distribution of local void fractions, with small and occasional bubbles contributing to the tail corresponding to the larger values of ϵ. As the gas superficial velocity is increased, a pronounced peak, representative of the bubble phase, appears at $\epsilon \cong 1$. The bubble-phase peak sharpens as $U - U_{mf}$ increases, keeping an almost constant voidage. As the gas superficial velocity increases, the distribution of voidages associated to the emulsion phase reveals a composite nature. The convolution of two modes becomes evident as a shoulder at first, emphasized as the gas superficial velocity increases to the point of

displaying two distinct peaks. The comparison of the PDF of the voidage signals recorded at different locations suggests that all the features become sharper at the upper level, H_2. Moreover, the contribution of the bubble phase to the PDF is larger at the upper level and along the axis of the bed under all the experimental conditions. This finding suggests that bubbles move toward the bed axis and coalesce during their uprise [51]. The contribution of the bubble phase to the PDF is larger at 500 °C than at room temperature.

The recognition of the composite, bimodal nature of the PDF component associated with the emulsion phase is very remarkable, and suggests that different phases with specific voidages co-exist in the emulsion phase: a lower voidage LV-phase and a higher voidage HV-phase. The peak voidages corresponding to either phase, respectively ϵ_{LV}^{mode} and ϵ_{HV}^{mode}, are plotted as a function of $U-U_{mf}$ in Fig. 8. Data points in this figure are reported for the two measurement levels, H_1 vs H_2, and for different temperatures, ambient vs 500 °C. Peak voidages ϵ_{LV}^{mode} and ϵ_{HV}^{mode} may be distinctively recognized only at excess gas superficial velocities $U-U_{mf}$ exceeding 0.1–0.2 m/s, and at specific bed axial/radial coordinates. In the other cases, the assessment of the two modal components, and of the associated peak values ϵ_{LV}^{mode} and ϵ_{HV}^{mode}, would require elaborated and possibly uncertain deconvolution procedures of the composite PDF, that have not been accomplished. So, at relatively low superficial gas velocities, where $\epsilon_{LV}^{mode} \cong \epsilon_{HV}^{mode}$, only one value has been plotted as emulsion phase voidage peak, ϵ_e^{mode}. At higher superficial gas velocities, where ϵ_{LV}^{mode} could not be distinctively recognized, but $\epsilon_{LV}^{mode} \neq \epsilon_{HV}^{mode}$, only ϵ_{HV}^{mode} has been plotted. Inspection of Fig. 8 suggests that ϵ_{LV}^{mode} is fairly constant, displaying only moderate departures from ϵ_{mf} throughout the range of excess gas superficial velocities investigated. On the contrary, the peak voidage of the HV-phase, ϵ_{HV}^{mode}, increases monotonically as $U-U_{mf}$ increases, approaching local bed voidages as large as 0.7. Again, Fig. 8 suggests that the bimodal character of the emulsion phase component of the PDF is sharper and better recognizable at H_2 for both temperatures.

In order to shed light on the physical nature of the HV- and LV-phases, the voidage time-series have been further analyzed to assess whether recurrent temporal patterns could be recognized. To this end, a closer scrutiny has been dedicated to events associated to the passage of bubbles. Fig. 9A reports a close-up sample of voidage time-series obtained in experiments carried out with the probe located at the bed axis, upper level, H_2, at ambient temperature and excess gas superficial velocity of $U-U_{mf} = 0.2m/s$. The selection of the probe location at the bed axis and at the upper level, H_2, was intentionally made to increase the probability that the probe is located along the uprise trajectory of individual bubbles. Data in Fig. 9A have been interpreted in the light of the representative pattern reported in Fig. 9B, where distinct stages typically associated with the bubble passage are represented. The PDF of the voidage time series is reported in Fig. 9C. A statistical analysis has been performed on the time series of bed voidage, by analyzing patterns associated to more than 50 bubble passages. Values of characteristic times in Fig. 9B have been obtained by determining the timings t_{down}^{**} and t_{up}^{**} at which the signal crosses the voidage ϵ^{**}, assumed as the threshold between the bubble and the emulsion phase, and the timings t_{down}^{*} and t_{up}^{*}

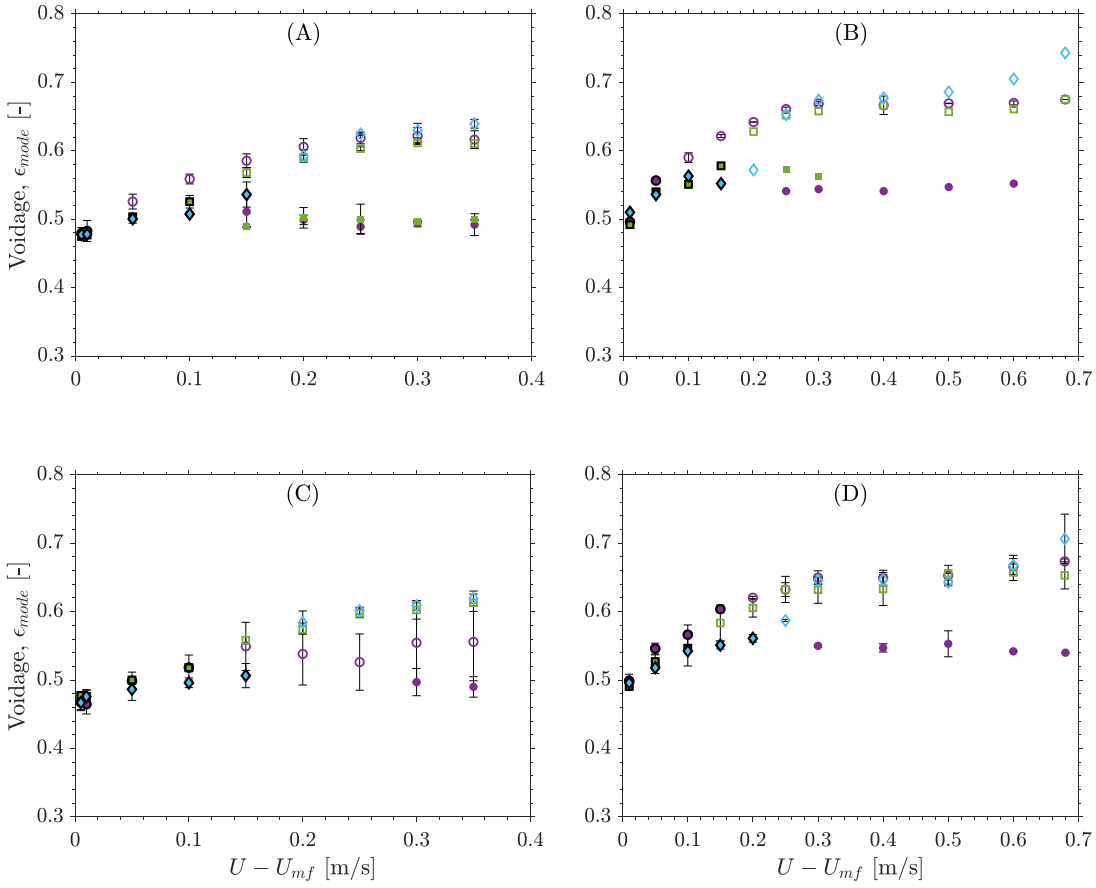

Fig. 8. Plot of peak voidages of the PDF for the HV- (hollow symbols) and LV- (non-edged full symbols) modal components (ϵ_{LV}^{mode} and ϵ_{HV}^{mode}, respectively) as a function of the excess gas superficial velocity $U-U_{mf}$. Where $\epsilon_{LV}^{mode} \cong \epsilon_{HV}^{mode}$, only one value as emulsion phase voidage peak, ϵ_e^{mode} (edged full symbols). (A) Probe level: H_2=0.1 m from distributor, T: ambient. (B) Probe level: H_2=0.1 m from distributor, T: 500 °C. (C) Probe level: H_1=0.06 m from distributor, T: ambient. (D) Probe level: H_1=0.06 m from distributor, T: 500 °C. Probe radial location: circles r/R = 0; squares r/R = 1/2; diamonds r/R = 7/9.

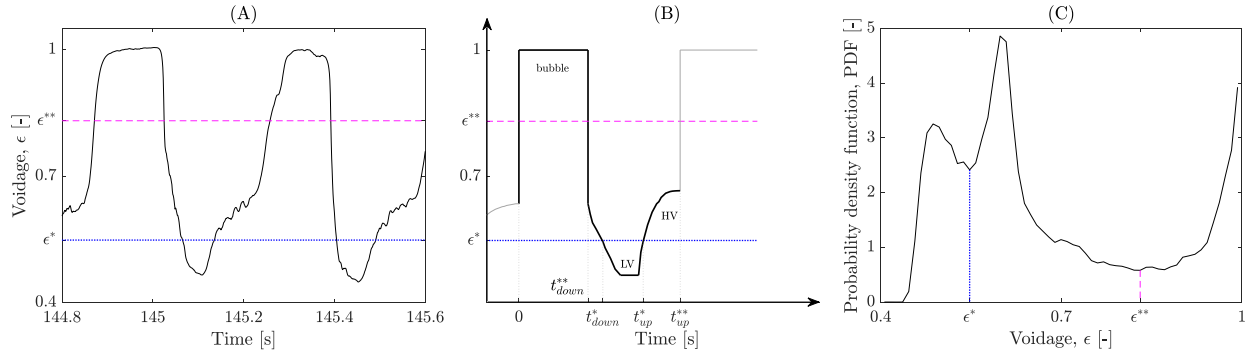

Fig. 9. (A) Sample of the time-resolved voidage signal. (B) Schematic pattern of the time resolved voidage associated with the passage of a bubble; (C) PDF of the time series. Operating conditions: ambient temperature, $U-U_{mf} = 0.2m/s$, probe location: bed axis, upper level ($H_2 = 0.1$ m from distributor).

at which the signal crosses the voidage ϵ^*, assumed as the threshold between the LV- and the HV-phases. Values of ϵ^* and ϵ^{**} have been taken as the minima in the PDF of Fig. 9C. The results of the statistical analysis are reported in Table 3. The entire cycle associated with a bubble passage, t^{**}_{up}, lasts, in the average 0.37 s. The time intervals during which the probe is in contact with the bubble, the LV-phase and the HV-phase are, in the average, 0.083 s, 0.037 s and 0.13 s, respectively. It is noteworthy that, on a statistical basis, $\left(t^{*}_{down}-t^{**}_{down}\right) \ll \left(t^{**}_{up}-t^{*}_{up}\right)$, a feature that suggests that the passage of the bubble is immediately followed by the detection of the LV-phase, eventually followed by the detection of a progressively more expanded state of the emulsion phase that reaches a maximum just before the arrival of a new bubble. This finding is consistent with the qualitative pattern represented in Fig. 9B, that implies the phenomenology associated to the passage of a bubble is characterized by the sequence Bubble → LV-phase → HV-phase. Moreover, the combined analysis of Fig. 9A and of the associated PDF in Fig. 9C suggests that the spectrum of bed voidages associated with the HV-phase is broader than the spectrum of the LV-phase.

These features represent the basis for a tentative inference of the physical nature of the LV- and HV-phases. It may be speculated that the HV-phase establishes in the emulsion phase as a consequence of shear flow induced by the passage of the bubble. The broad spectrum of voidages would reflect different values of the local shear rates, that reach a maximum as a rising bubble approaches the probe. Accordingly, expansion of the emulsion phase in the proximity of bubbles would reflect the well established dilatancy of dense granular flows subject to shear. In this framework, the LV-phase immediately trailing the bubble should correspond to solids located in the bubble wake, characterized by prevailingly coherent translational motion and no shear. Of course, at small excess gas superficial velocities the emulsion phase would be predominantly undisturded by the bubble passage and a fairly narrow range of local bed voidages typical of the LV-phase ($\approx \epsilon_{mf}$) would establish throughout the bed. Altogether, it may be concluded bubble-induced shear might be responsible for the establishment of an expanded state of the emulsion phase at voidages well exceeding ϵ_{mf} to an extent that increases with increasing excess gas superficial velocity $\left(U-U_{mf}\right)$.

Table 3
Characteristic times of the voidage time series. Operating conditions: ambient temperature, $U-U_{mf} = 0.2m/s$, probe location: bed axis, upper level (H_2).

Time [s]	
t^{**}_{up}	0.374 ± 0.077
$t^{*}_{up}-t^{*}_{down}$	0.083 ± 0.023
$t^{*}_{down}-t^{**}_{down}$	0.037 ± 0.042
$t^{**}_{up}-t^{*}_{up}$	0.131 ± 0.054
$t^{**}_{down} \cong t_b$	0.122 ± 0.044

3.2. Mass transfer-limited reaction experiments

Results of experiments aimed at measurement of the mass transfer coefficient under reaction conditions are reported in Fig. 10. The values of the Sherwood number measured during catalytic oxidation of CO are plotted as a function of the excess gas superficial velocity $\left(U-U_{mf}\right)$. For each operating condition, data points were averaged over three independent experiments. The experimental procedure closely reflects that adopted by Scala [13], but the larger inner diameter of the present experimental apparatus prevents the onset of slugging, so that all the experiments were carried out under freely bubbling conditions.

The Frössling-type Eq. (1), whose validity has been discussed by Scala [13], is typically used to calculate the Sherwood number to express mass transfer to active particles in bubbling fluidized beds. Values of *Sh* computed using Eq. (1) are plotted in Fig. 10 for comparison with experimental data. It is noteworthy that the Sherwood numbers obtained from the experiments increase with increasing fluidization velocity, whereas *Sh* calculated from Eq. (1) is fairly constant. This discrepancy can be explained considering the results obtained in the previous section, in the light of the bubble-induced expansion of the emulsion phase. Consistently with results of Scala [13], the catalyst particles, whose size largely exceeds that of the inert bed particles, mostly reside in the emulsion phase of the fluidized bed. Correspondingly, computations of *Sh* must be based on the value of the voidage that

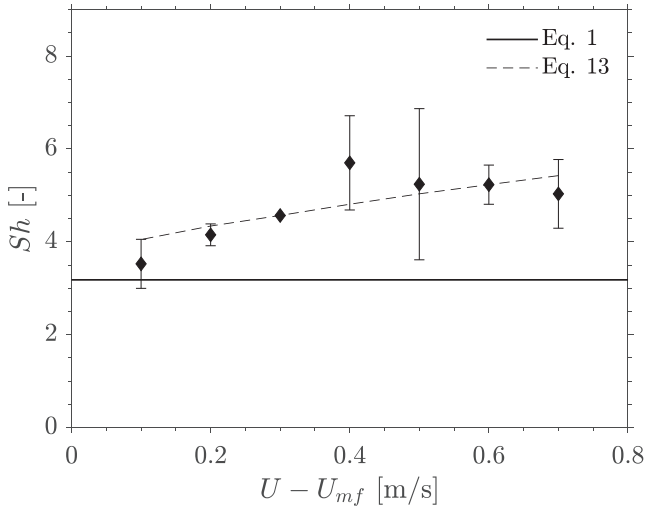

Fig. 10. Sherwood number as a function of excess gas superficial velocity. T = 450 °C; bed material: grey quartz sand. Frössling-type correlations: Eq. (1) (continuous line), K=0.70; Eq (13) (dashed line), K=0.84.

is actually established in the emulsion phase. The expanded state of the emulsion phase as the excess gas superficial velocity increases, reported and discussed in the previous section, must be taken into account in the computations. Accordingly, Eq. (1) has been modified into:

$$Sh = 2\cdot\epsilon_e + K\cdot(Re_e/\epsilon_e)^{1/2}\cdot Sc^{1/3} \tag{13}$$

where $Re_e = \rho_g\cdot U_e\cdot d_p^a/\mu_g$, and ϵ_e and U_e are the effective voidage, and gas velocity of the emulsion phase, respectively. The value of U_e is estimated from the correlation reported by Hilligardt and Werther for three-dimensional beds [31]:

$$\frac{U_e - U_{mf}}{U - U_{mf}} = \frac{1}{3} \tag{14}$$

The value of ϵ_e is taken as the voidage of HV-phase averaged over the column cross-section and bed height for each gas superficial velocity, obtained according to the experimental procedure reported in section *2.3.2*. Fitting Eq. (13) against experimental results reported in Fig. 10 yields $K = 0.84$. Equation (13), with ϵ_e and U_e estimated as reported above, is plotted in Fig. 10. The good agreement of values of *Sh* computed with Eq. (13) with the experimental data points confirms the validity of the assumption that the expanded state of the emulsion phase must be taken into account in the calculation of the effective Sherwood number, and provides additional confirmation of the expansion of the emulsion phase of the bed at increasing gas superficial velocity.

Sh, according to Eq. (13), is composed of two additive contributions associated with the diffusive (Sh_{diff}) and convective (Sh_{conv}) terms of mass transfer, respectively. Fig. 11 reports the values of the two components as a function of $U - U_{mf}$, using the spatially averaged voidage of HV-phase, according to the experimental procedure reported in section *2.3.2*, and $K = 0.84$. It can be observed that: i) Sh_{conv} always exceeds Sh_{diff}; ii) Sh_{conv} and Sh_{diff} increase linearly with $U - U_{mf}$; iii) the slope of Sh_{conv} is 4.5 times higher than that of Sh_{diff}. Overall, the comparison of the two curves highlights that Sh_{conv} represents the major contribution of *Sh* and its relevance becoming higher as $U - U_{mf}$ is increased. As matter of fact, Sh_{diff} is limited by the effective voidage of the emulsion phase, which does not exceed 0.69 in the results reported in the present experimental campaign. Instead, Sh_{conv} mainly depends on the effective gas velocity in the emulsion phase, which steadily increases with $U - U_{mf}$.

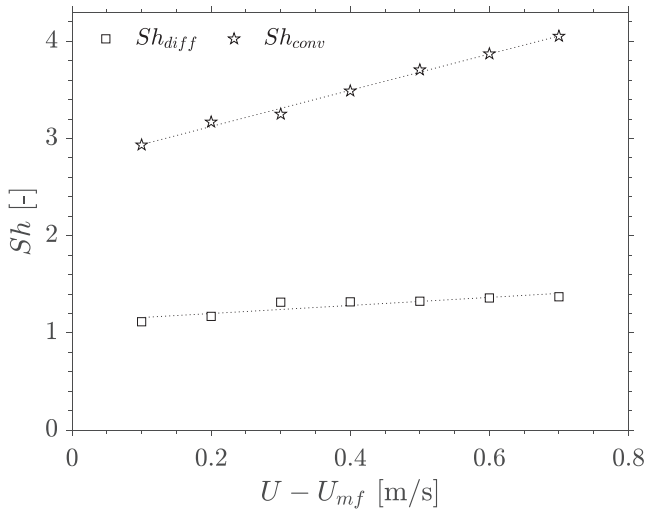

Fig. 11. Diffusive and convective contributions to Sherwood number versus excess superficial gas velocity with respect to incipient fluidization conditions.

4. Conclusions

Capacitance probes have been successfully utilized to characterize the hydrodynamics of Geldart-B solids dense fluidized beds operated at ambient and high temperature. The custom-made probes have displayed excellent durability, working for more than 200 h at 500 °C, under the mechanical action of the fluidizing particles, without noticeable alteration of the capacitance signal. Different locations of the probes permitted to obtain spatial maps of time-resolved pointwise values of the bed voidage, which were consistent with independently derived values of the overall bed voidage.

Statistical analysis of the time-series of local bed voidage yields probability density functions (PDF) that display multimodal patterns. A remarkable bimodal character is apparent in the portion of the spectrum that refers to the emulsion phase of the bed, more pronounced as the gas superficial velocity is increased. It is inferred that different phases at distinctively different voidage co-exist in the emulsion phase: a lower voidage LV-phase and a higher voidage HV-phase. A detailed analysis of selected time series was accomplished, with the aim of inferring the physical nature of the LV- and HV-phases. It is speculated that the LV-phase, which is detected by the probes immediately after the passage of the bubble, may be associated with the wake of the bubble, whereas the HV-phase may be representative of the bulk of the emulsion phase. It is further speculated that the expanded state of the HV-phase, above the voidage of the incipiently fluidized bed, may be the consequence of bed dilatancy associated with bubble-induced shear flow.

Although results obtained at 500 °C qualitatively resemble those obtained at ambient temperature, quantitative differences are observed, confirming the need for characterization of bed hydrodynamics at temperatures of interest in industrial applications.

A dedicated campaign consisting of fluidized bed catalytic oxidation of CO has been directed to the assessment of the mass transfer coefficient between the bulk of the bed and active particles, under the assumption of infinitely fast chemical kinetics. Results are fully consistent with the experimental findings obtained from the hydrodynamic characterization of the bed at comparable temperature. In particular, it is shown that better estimates of the active particle Sherwood number *Sh* are obtained if the Frössling equation is implemented using the actual voidage of the expanded emulsion phase, rather than the voidage corresponding to incipient fluidization. This analysis is relevant to the assessment of bed-particle mass transfer coefficients controlling the apparent reaction rate in the fast-chemical reaction regime. This regime is frequently encountered in many fluidized bed processes aimed at thermochemical conversion of solid fuels.

CRediT authorship contribution statement

Laura Molignano: Conceptualization, Methodology, Software, Validation, Formal analysis, Investigation, Writing – original draft, Visualization. **Maurizio Troiano:** Supervision, Conceptualization, Writing - review & editing. **Roberto Solimene:** Conceptualization, Methodology, Resources, Writing – review & editing, Project administration, Supervision, Funding acquisition. **Sina Tebianian:** Supervision, Conceptualization, Writing - review & editing. **Fabrizio Scala:** Methodology, Resources, Writing – review & editing. **Piero Salatino:** Conceptualization, Writing – review & editing, Visualization, Funding acquisition, Supervision. **Jean-François Joly:** Funding acquisition, Supervision.

Declaration of Competing Interest

The authors declare that they have no known competing financial interests or personal relationships that could have appeared to influence the work reported in this paper.

Data availability

Data will be made available on request.

Acknowledgments

The authors gratefully acknowledge Mr Antonio Cammarota for the set-up of the experimental apparatus and Prof. David Pallarès for the useful discussion on mass transfer at FBC24 conference.

References

[1] Kwong KY, Marek EJ. Combustion of Biomass in Fluidized Beds: A Review of Key Phenomena and Future Perspectives. Energy Fuel 2021;35:16303–34. https://doi.org/10.1021/acs.energyfuels.1c01947.
[2] Hofbauer H, Rauch R, Bosch K, Koch R, Aichernig C. Biomass CHP Plant Güssing - A Success Story. Expert Meet Pyrolysis Gasif Biomass Waste 2003:527–36.
[3] Motta IL, Miranda NT, Maciel Filho R, Wolf Maciel MR. Biomass gasification in fluidized beds: A review of biomass moisture content and operating pressure effects. Renew Sustain Energy Rev 2018;94:998–1023. https://doi.org/10.1016/j.rser.2018.06.042.
[4] Troiano M, Ianzito V, Solimene R, Ganda ET, Salatino P. Fluidized Bed Pyrolysis of Biomass: A Model-Based Assessment of the Relevance of Heterogeneous Secondary Reactions and Char Loading. Energy Fuel 2022;36:9660–71. https://doi.org/10.1021/acs.energyfuels.2c01483.
[5] Adánez J, Abad A. Chemical-looping combustion: Status and research needs. Proc Combust Inst 2019;37:4303–17. https://doi.org/10.1016/j.proci.2018.09.002.
[6] Salatino P, Solimene R. Mixing and segregation in fluidized bed thermochemical conversion of biomass. Powder Technol 2017;316:29–40. https://doi.org/10.1016/j.powtec.2016.11.058.
[7] Li T, Thunman H, Ström H. A fast-solving particle model for thermochemical conversion of biomass. Combust Flame 2020;213:117–31. https://doi.org/10.1016/j.combustflame.2019.11.018.
[8] Troiano M, Cammarota A, Tregambi C, Chirone R, Salatino P, Solimene R. Fluidized bed combustion of solid lignin-rich residues from bioethanol production. Powder Technol 2020;371:170–9. https://doi.org/10.1016/j.powtec.2020.05.070.
[9] Kwong KY, Mao R, Scott SA, Dennis JS, Marek EJ. Analysis of the rate of combustion of biomass char in a fluidised bed of CLOU particles. Chem Eng J 2021;417:127942. https://doi.org/10.1016/j.cej.2020.127942.
[10] Hayhurst AN, Parmar MS. Measurement of the mass transfer coefficient and sherwood number for carbon spheres burning in a bubbling fluidized bed. Combust Flame 2002;130:361–75. https://doi.org/10.1016/S0010-2180(02)00387-5.
[11] Scala F. A new technique for the measurement of the product CO/CO2 ratio at the surface of char particles burning in a fluidized bed. Proc Combust Inst 2009;32(II):2021–7. https://doi.org/10.1016/j.proci.2008.06.047.
[12] Johnstone H, Toomey R. Gas fluidization of solid particles. Chem Eng Prog 1952;48:220–6.
[13] Scala F. Mass transfer around freely moving active particles in the dense phase of a gas fluidized bed of inert particles. Chem Eng Sci 2007;62:4159–76. https://doi.org/10.1016/j.ces.2007.04.040.
[14] Van Ommen JR, Mudde RF. Measuring the gas-solids distribution in fluidized beds - A review. Int J Chem React Eng 2008;6:1–29. https://doi.org/10.2202/1542-6580.1796.
[15] Martinez Castilla G, Larsson A, Lundberg L, Johnsson F, Pallarès D. A novel experimental method for determining lateral mixing of solids in fluidized beds – Quantification of the splash-zone contribution. Powder Technol 2020;370:96–103. https://doi.org/10.1016/j.powtec.2020.05.036.
[16] Yates JG, Cheesman DJ, Lettieri P, Newton D. X-ray analysis of fluidized beds and other multiphase systems. KONA Powder Part J 2002. https://doi.org/10.14356/kona.2002016.
[17] Lettieri P, Yates JG. New Generation X-ray Imaging for multiphase systems. 14th Int Conf Fluid – From Fundam to Prod 2013:641–8.
[18] Penn A, Boyce CM, Kovar T, Tsuji T, Pruessmann KP, Müller CR. Real-Time Magnetic Resonance Imaging of Bubble Behavior and Particle Velocity in Fluidized Beds. Ind Eng Chem Res 2018;57:9674–82. https://doi.org/10.1021/acs.iecr.8b00932.
[19] Dubrawski K, Tebianian S, Bi HT, Chaouki J, Ellis N, Gerspacher R, et al. Traveling column for comparison of invasive and non-invasive fluidization voidage measurement techniques. Powder Technol 2013;235:203–20. https://doi.org/10.1016/j.powtec.2012.10.031.
[20] Tebianian S, Dubrawski K, Ellis N, Cocco RA, Hays R, Reddy Karri SB, et al. Investigation of particle velocity in FCC gas-fluidized beds based on different measurement techniques. Chem Eng Sci 2015;127:310–22. https://doi.org/10.1016/j.ces.2015.01.049.
[21] Velarde IC, Gallucci F, van Sint AM. Development of an endoscopic-laser PIV/DIA technique for high-temperature gas-solid fluidized beds. Chem Eng Sci 2016;143:351–63. https://doi.org/10.1016/j.ces.2016.01.002.
[22] Hernberg R, Stenberg J, Zethræus B. Simultaneous in situ measurement of temperature and size of burning char particles in a fluidized bed furnace by means of fiberoptic pyrometry. Combust Flame 1993;95:191–205. https://doi.org/10.1016/0010-2180(93)90061-7.
[23] Johnsson H, Johnsson F. Measurements of local solids volume-fraction in fluidized bed boilers. Powder Technol 2001;115:13–26. https://doi.org/10.1016/S0032-5910(00)00270-9.
[24] Wiesendorf V, Werther J. Capacitance probes for solids volume concentration and velocity measurements in industrial fluidized bed reactors. Powder Technol 2000;110:143–57. https://doi.org/10.1016/S0032-5910(99)00276-4.
[25] Tebianian S, Ellis N, Lettieri P, Grace JR. X-ray imaging for flow characterization and investigation of invasive probe interference in travelling fluidized bed. Chem Eng Res Des 2015;104:191–202. https://doi.org/10.1016/j.cherd.2015.08.006.
[26] Hage B, Werther J. The guarded capacitance probe - A tool for the measurement of solids flow patterns in laboratory and industrial fluidized bed combustors. Powder Technol 1997;93:235–245. https://doi.org/10.1016/S0032-5910(97)03276-2.
[27] Campbell CS, Wang DG. A particle pressure transducer suitable for use in gas-fluidized beds. Meas Sci Technol 1990;1:1275–9. https://doi.org/10.1088/0957-0233/1/12/002.
[28] Solimene R. Mixing and Segregation in Fluidized Beds. Ref Modul Chem Mol Sci Chem Eng 2017. https://doi.org/10.1016/b978-0-12-409547-2.12186-9.
[29] Olsson J, Pallarès D, Johnsson F. Lateral fuel dispersion in a large-scale bubbling fluidized bed. Chem Eng Sci 2012;74:148–59. https://doi.org/10.1016/j.ces.2012.02.027.
[30] Abrahamsen AR, Geldart D. Behaviour of gas-fluidized beds of fine powders part I. Homogeneous expansion Powder Technol 1980;26:35–46. https://doi.org/10.1016/0032-5910(80)85005-4.
[31] Hilligardt K, Werther J. Influence of temperature and properties of solids on the size and growth of bubbles in gas fluidized beds. Chem Eng Technol 1987;10:272–80. https://doi.org/10.1002/ceat.270100133.
[32] Glicksman LR, McAndrews G. The effect of bed width on the hydrodynamics of large particle fluidized beds. Powder Technol 1985;42:159–67. https://doi.org/10.1016/0032-5910(85)80049-8.
[33] Cui H., Mostoufi N., Chaouki J. Characterization of dynamic gas-solid distribution in fluidized beds 2000;79:133–143.doi:10.1016/S1385-8947(00)00178-9.
[34] Andreux R, Chaouki J. Behaviors of the bubble, cloud, and emulsion phases in a fluidized bed. AIChE J 2008;54:406–14. https://doi.org/10.1002/aic.11390.
[35] Formisani B, Girimonte R, Pataro G. The inf luence of operating temperature on the dense phase properties of bubbling f luidized beds of solids. Powder Technol 2002;125:28–38. https://doi.org/10.1016/S0032-5910(01)00494-6.
[36] Cui H, Chaouki J. Effects of temperature on local two-phase flow structure in bubbling and turbulent fluidized beds of FCC particles. Chem Eng Sci 2004;59:3413–22. https://doi.org/10.1016/j.ces.2004.05.006.
[37] Shabanian J, Chaouki J. Effects of temperature, pressure, and interparticle forces on the hydrodynamics of a gas-solid fluidized bed. Chem Eng J 2017;313:580–90. https://doi.org/10.1016/j.cej.2016.12.061.
[38] Kunii D, Levenspiel O. Fluidization and Mapping of Regimes. Fluid Eng 1991:61–94. https://doi.org/10.1016/b978-0-08-050664-7.50009-3.
[39] Knowlton TM. In: Pressure and temperature effects in fluid-particle systems. New York: Engineering Foundation; 1992. p. 27–46. Fluid. 7.
[40] Formisani B, Girimonte R, Mancuso L. Analysis of the fluidization process of particle beds at high temperature. Chem Eng Sci 1998;53:951–61. https://doi.org/10.1016/S0009-2509(97)00370-9.
[41] Grace JR. Properties, Minimum Fluidization, and G eldart Groups. Essentials Fluid Technol 2020:11–32. https://doi.org/10.1002/9783527699483.ch2.
[42] Yang W-C. Flow through fixed beds. Handb Fluid fluid-particle Syst 2003:29–52. https://doi.org/10.1016/s1672-2515(07)60126-2.
[43] Riley CA, Louge M. Quantitative capacitive measurements of voidaqe in gas-solid flows. Part Sci Technol 1989;7:51–9. https://doi.org/10.1080/02726358908906523.
[44] Montgomery DC, Runger GC. Applied Statistics and Probability for Engineers. 7° edition. New York: 2018.
[45] Clift R, Grace JR. Continuous bubbling and slugging. In: Academic Press, editor. Fluidization. second, London: 1985.
[46] Darton RC, La Nauze RD, Davidson J, Harrison H. Bubble growth due to coalescence in fluidised beds. T I Chem Eng-L 1977;55:274–80.
[47] Venderbosch RH, Prins W, Van Swaaij WPM. Platinum catalyzed oxidation of carbon monoxide as a model reaction in mass transfer measurements. Chem Eng Sci 1998;53:3355–66. https://doi.org/10.1016/S0009-2509(98)00151-1.
[48] Falkowski D, Brown RC. Analysis of pressure fluctuations in fluidized beds. Ind Eng Chem Res 2004;43:5721–9. https://doi.org/10.1021/ie030684u.
[49] Sit SP, Grace JR. Effect of bubble interaction on interphase mass transfer in gas fluidized beds. Chem Eng Sci 1981;36:327–35. https://doi.org/10.1016/0009-2509(81)85012-9.
[50] Werther J, Molerus O. The local structure of gas fluidized beds -I. A statistically based measuring system. Int J Multiph Flow 1973;1:103–122. https://doi.org/10.1016/0301-9322(73)90007-4.
[51] Werther J, Molerus O. The local structure of gas fluidized beds -II. The spatial distribution of bubbles. Int J Multiph Flow 1973;1:123–38. https://doi.org/10.1016/0301-9322(73)90008-6.